Journal of Power Sources 551 (2022) 232214

Contents lists available at ScienceDirect

Journal of Power Sources

journal homepage: www.elsevier.com/locate/jpowsour

Thermal management system for air-cooled battery packs with flow-disturbing structures

R. Cagtay Sahin, Sinan Gocmen, Erdal Cetkin *

Department of Mechanical Engineering, Izmir Institute of Technology, Gulbahce, Urla, Izmir, 35430, Turkey

HIGHLIGHTS

- P3D thermal model is documented for a cell and validated through experiments.
- Results of cell and module level simulations and experiments are documented.
- The cooling performance can be improved by inserting spoilers.
- Staggered layouts yield better thermal performance relative to inline arrangements.
- Parasitic power consumption and cooling performance of designs are documented.

ARTICLE INFO

Keywords:
Battery thermal management system
P3D model
Temperature uniformity
Forced air convection
Cylindrical lithium-ion battery
Winglets

ABSTRACT

Lithium-ion battery packs are preferred in electrical vehicles (EVs) due to their efficient and stable characteristics. Battery thermal management systems (BTMS) have vital importance in EVs to keep batteries in the desired temperature range to maximize performance and lifetime. BTMS with air cooling is simpler and lighter relative to competing methods; however, low thermal conductivity and heat capacity of air necessitate thermal performance and pressure drop adjustments. This work offers a novel design method for cylindrical cells by evaluating the effect of various baffles (cylindrical, triangular, diamond and winglet) on the cooling performance and pressure drop of an air-cooled battery module with 12 21700 cylindrical cells. Thermal characteristics are simulated by the electrochemical-thermal battery model, the P3D multiscale model (modelling parameters for a commercial 21700 cell are documented) in COMSOL Multiphysics 5.5 and their accuracy is validated by experiments. As a result, baffles reduce the maximum temperature and temperature difference by 5% (1.8 °C) and 40% (1.7 °C), respectively, consuming 3.5 times more power than the base design. Delta winglets offer the optimum solution, reducing the maximum temperature and temperature difference by 2% (0.6 °C) and 15% (0.7 °C), respectively, with a 44% (0.12 W) rise in parasitic power consumption.

1. Introduction

Recently, due to climate change, electrical and hybrid vehicles (EVs and HEVs) have gained tremendous importance in recent years, as they are the cleanest options in terms of global warming emissions [1,2]. In addition, many vehicle manufacturers have announced that they will not produce internal combustion engine vehicles soon (i.e., 2030). Therefore, the importance of EVs and HEVs has increased exponentially, which has paved the road for the basis for numerous academic studies on the efficiency and sustainability of electric vehicles. Since the efficiency, cost and lifespan of EVs are affected greatly from the batteries [3], the literature has many studies on improving the performance, longevity and safety of cells and battery packs. In addition, EVs require batteries that do not suffer from memory effect as regenerative braking causes sporadically changing charge/discharge cycles while driving. Briefly, EVs and HEVs require batteries with low self-discharge rates and high energy density that are not suffering from the memory effect. Hence, the prominence of lithium-ion batteries is self-evident compared to other types of batteries [4].

However, the internal structure of lithium-ion batteries is affected by side reactions and these reactions depend on temperature [5]. Due to side reactions, irreversible and critical phenomena such as dendrite growth, available capacity retention, accelerated aging effects and thermal runaway (TR) may occur [6]. Internal changes or external improvements can slow down these side reactions. As for the internal

* Corresponding author.
E-mail address: erdalcetkin@iyte.edu.tr (E. Cetkin).

https://doi.org/10.1016/j.jpowsour.2022.232214
Received 2 August 2022; Received in revised form 29 September 2022; Accepted 3 October 2022
Available online 13 October 2022

Nomenclature

A	polynomial coefficients
a_s	effective surface area [m^{-1}]
c	lithium concentration [mol m^{-3}]
d_{can}	thickness of battery casing [mm]
C_μ	turbulence model constant
$C_{\varepsilon 1}$	turbulence model constant
$C_{\varepsilon 2}$	turbulence model constant
Cp	specific heat capacity [J kg^{-1} K^{-1}]
D	diffusion coefficient [m^2 s^{-1}]
$D_{hydraulic}$	hydraulic diameter [m]
E_{eq}	equivalent potential [V]
f	friction factor
$f_\pm$	molar salt activity coefficient
F	Faraday constant [C mol^{-1}]
h	convective heat transfer coefficient [W m^{-2} K^{-1}] and battery height [m]
i_0	reference exchange current density [A m^{-2}]
i	current density [A m^{-2}]
I_{app}	applied current to battery [A m^{-2}]
j^{Li+}	reaction current density [A m^{-2}]
k	thermal conductivity [W m^{-1} K^{-1}] or turbulent kinetic energy [m^2 s^{-2}]
l_T	turbulent length scale [m]
L_T	characteristic length [m]
L	battery layer length [μm]
N_{batt}	number of batteries
N	number of data points
Nu	Nusselt number
P_{out} *and* P_{in}	outlet and inlet pressure [Pa] P_k outlet and inlet pressure [Pa] P_k production number
P_{fan}	fan power consumption [W]
P_{Vol}	volumetric power efficiency [W l^{-1}]
Q	heat generation rate [W m^{-3}]
r	radius [m] or [μm] in electrochemical model
r_p	particle radius [μm]
R	universal gas constant [J mol^{-1} K^{-1}]
Re	Reynolds number
SoC	state of charge
S_x *and* S_L	battery distance in flow direction [mm] S_y *and* S_T battery distance in transverse direction [mm] t_+^0 battery distance in flow direction [mm] S_y *and* S_T battery distance in transverse direction [mm] t_+^0 transference number
T	temperature [°C]
U_0	inlet velocity [m/s]
x	coordinate and cathode SoC
y	anode SoC

Greek letters

α	transfer coefficient
β	Bruggemann tortuosity coefficient
δ	cell-to-cell distance [mm]
$\overline{\delta}$	mean absolute error between simulation and experiment
Δ	nabla operator
ΔT	temperature difference [°C]
ε	volume fraction rate and turbulence dissipation rate [m^2 s^{-3}]
η	overpotential [V]
κ	ionic conductivity [S m^{-1}]
μ	kinematic viscosity [m^2 s^{-1}]
ρ	density [kg m^{-3}]
σ	electronic conductivity [S m^{-1}]
σ_k	turbulent flow constant
σ_ε	turbulent flow constant
Φ	potential [V]

Subscripts and Superscripts

amb	ambient conditions
batt	battery
eff	effective
in	inlet
irr	irreversible
l	liquid state
neg	negative electrode
ohm	ohmic
out	outlet
pos	positive electrode
rev	reversible
s	solid state
sep	separator
tang	tangential
tot	total
T	turbulence

alterations, manufacturers can use more reliable and less pollutant materials to increase thermal and electrochemical stability of cells or adopt some additives to improve these features of battery materials. Since electrolytes predominantly participate in chemical reactions, their interactions between cathode and anode materials are as important as the ionic conductivity and stability of the material. Electrolytes that are less prone to catching fire, not creating lithium plating and forming stable solid/cathode electrolyte interface (SEI/CEI) layers are the goals of safe battery operation [7]. Highly-saturated electrolytes can inhibit the reactions between organic materials and electrodes which improves stability [8]. Self-healing materials can extend the lifecycle and enhance the ability to survive the mechanical damage of a battery [9]. Also, the performance of solid electrolytes, which is a promising option for safe batteries, can be increased by distinct additives [10]. Another method for mitigating TR is improving thermal and chemical stability of cathode materials, as they release a significant amount of oxygen in case of decomposition [11]. In addition, nickel-rich cathode compositions are important as they contribute to the commercialization of lithium metal batteries and offer a cleaner and cheaper alternative for cobalt compounds [12]. Ultimately, the chemical and physical properties of anode materials also affect battery safety. Alongside the flammability of carbon compounds in the anode, it affects safety by having unstable thermal characteristics and a weak SEI layer. Stable carbon structures [13], coatings and electrolyte additives creating robust SEI films are studied to overcome such bottlenecks [14].

In addition to the material research, improved operating conditions significantly affect health, safety and longevity of batteries. The temperature range between 20 °C and 40 °C is a safe operating zone for lithium-ion batteries [15]. Additionally, uniform temperature distribution in a battery pack is another objective that needs attention because of the aging characteristics of batteries heavily depend on temperature [16]. Briefly, over-charge and over-discharge may lead to dendrite growth and anode current collector dissociation [17]. Hence, all the cells in a pack must operate in a temperature range that does not exceed 5 °C to avoid over-charging or over-discharging [16–18].

For these reasons, under an operation where batteries are stacked together to work under aggressive charge/discharge cycles, EVs and HEVs require thermal management (BTMS) and battery management

(BMS) systems to ensure safety and increase efficiency in vehicles. Briefly, battery management strategies involve the state of health/charge estimations [19–21] and adaptive control systems [22,23]. BTMSs deal with cell placements, cooling strategies and cooling optimizations. Pesaran et al. [3] studied the possible cooling methods for EV applications by evaluating their properties and limitations. BTMSs can be classified based on their cooling techniques, namely passive and active cooling. Air cooling, liquid cooling and immersion cooling are active, and heat pipes, PCM and natural convection are passive methods. There are also various hybrid systems which combine active and passive methods.

The active methods intrinsically are the most effective ones. For example, air cooling offers lightweight and straightforward designs. Without extra channels or jackets, as required in liquid cooling, the maintenance and manufacturing costs of air-cooled BTMS are relatively low [24]. However, because of the lower heat capacity and thermal conductivity of air, the cooling performance of these systems is not efficient for high C-rates. Hence, air cooling applications are favorable for EVs with short-range and low power output [25].

Air-cooled BTMS literature focuses on optimizing parameters to enhance cooling performance and temperature uniformity. Varying flow characteristics, altering manifold design and re-organizing cells are some methods available in the literature. With the consideration of low thermal conductivity and heat capacity of air, cooling design optimizations by varying airflow characteristics is a mandatory option as it compensates these downsides. However, these alterations may have side effects, such as pressure drop, power consumption and noise [26]. Sabbah et al. [27] compared the phase change material (PCM) and the air cooling for a pack and found that air cooling in the laminar region is inadequate when the ambient temperature is 45 °C. Mahamud et al. [28] adopted a novel airflow strategy and it decreased the temperature gradient by 72% and the contribution of cell arrangements to the cooling was 10%. Saw et al. [15] experimentally and numerically investigated the cooling performance of a battery pack. They reduced the maximum temperature and temperature difference by 37% and 66%, increasing the fan power by 0.6 W. Chen et al. [29] compared the cooling performance of air cooling, fins, cold plate and direct liquid cooling by comparing battery temperature and pressure drop data. Their results show that air cooling consumes more power than others to provide an equal heat rejection for the considered cases. Yu et al. [30] experimentally optimized the axial air cooling method for a battery pack with 66 cylindrical cells by varying the flow rate. The literature shows that alongside the power consumption, cooling performance limits the optimum flow rate as its effectiveness gradually decreases.

Altering manifold design is an option in favor of achieving uniform air distribution among cells, as equally distributed air to each cell is another objective for air-cooled BTMSs [24]. In addition, repositioning of inlet and outlet significantly affects cooling performance [31]. Using numerical methods, Xie et al. [32] employed an orthogonal array testing technique to understand the effect of inlet/outlet widths and angles. The best design yielded 13% lower maximum temperature and 30% more uniform temperature gradient than the base design. Shahid et al. [33] extended the inlet to provide extra air to the hotspots by changing air direction with inserted planes. This yielded 8% better cooling with 25% more uniform temperature distribution than their base design. Na et al. [34] decreased the temperature gradient by 47% and the maximum temperature by 2.7 °C with a configuration of two inlets on opposite sides. Jiaqiang et al. [35] reduced 26% of the maximum temperature by changing inlet and outlet positions and inserting baffles. Jilte et al. [36] improved the cooling performance of a pack by locating each module in a confined air channel, which reduced the maximum temperature by around 18%. Zhou et al. [37] introduced a design where air was injected into the battery pack through perforated pipes and it yielded the desired performance even at 5C discharge rate.

Cell arrangements are necessary for acquiring volumetric power efficiency and cooling improvements. Furthermore, the pressure drop is another variable that needs attention while changing cell layouts. Gocmen et al. [38] optimized the mass flow rates in between batteries by varying cell positions based on constructal theory [39] and it reduced the maximum temperature and temperature gradient by 60% and 97%, respectively. Yang et al. [40] compared the cooling performances of staggered and inline layouts and they documented that inline alignment yields better performance in terms of temperature gradient. In contrast, the staggered design reduces the maximum temperature the most. Lu et al. [41] investigated the effect of various flow rates and cell distances on the thermal performance of a battery pack with 252 cells. While the former reduced the maximum temperature by 26%, the latter decreased it by 35%. Yang et al. [42] designed a system which acquired a 47% more homogenous temperature gradient and 16% lower maximum temperature with a loss of 27% space efficiency and this design consumed 95% less parasitic power. Han et al. [26] numerically investigated required volume flow rate of a battery pack for various scenarios and they documented the effect of winglet parameters on the cooling of prismatic cells. As a result, they explained the limitations of air-cooling systems and the effectiveness of winglet vortex generators.

In conclusion, in air-cooled BTMS literature, many studies focus on cooling improvements by optimizing cell arrangements, flow characteristics and manifold designs. However, as interpreted from those studies, the effect of these alterations is limited by power consumption and space efficiency. In addition, as a result of these applications, unused air regions can still be seen, causing some cold air to leave the chamber without absorbing heat. Also, there is a scarcity of studies investigating the effectiveness of baffle structures, which is a universal application in heat exchangers. Therefore, flow-disturbing structures can significantly improve the cooling performance when combined with other techniques. This paper analyses the effect of several flow-disturbing structures (cylindrical/triangular/diamond shaped spoilers and vortex generators) on the cooling performance of a module consisting of 12 cylindrical lithium-ion cells. Initially, a module consisting of 6 cells in a 2P3S connection was simulated by utilizing a P3D electrochemical-thermal model of lithium-ion cells. Then, an experiment was conducted to validate the accuracy of the battery module simulation. Finally, the thermal effectiveness of several design layouts was assessed with a 3D CFD simulation of a battery module with 12 cells connected in a 6S2P arrangement. In conclusion, thermal performance of several distinct approaches has been compared via numerical simulations, where the maximum temperature, temperature uniformity and pressure drop data are documented.

2. Model and method

This study aims to acquire a reliable simulation for a battery module including a dozen cells to enhance the cooling performance. For this purpose, experiments are conducted to validate the cell and module level simulations. In the experiments, six cells connected with 2P3S layout are placed in a plexiglass shell with airflow supplied by an AC fan. The simulations comprise 3D turbulent airflow and heat transfer coupled with a 1D electrochemical-thermal battery model. While a stationary solver is used for uncovering the flow field, heat transfer and battery models are solved by a time-dependent solver in COMSOL Multiphysics 5.5. Inlet velocity and temperature are 1.6 m/s and 20 °C and the initial temperature of each component are equal to the inlet temperature, i.e. 20 °C. The cell is a commercially available 21700 cylindrical lithium-ion cell (capacity = 4200 mAh, maximum voltage = 4.2V and minimum voltage = 2.5V) [43]. The cell dimensions are given in Table 1 with descriptions.

Battery cells are placed in staggered and inline alignments with 7 and 15 mm cell-to-cell distances. Furthermore, distinct types of baffles (cylindrical, diamond, triangle and winglet) are located in between the cells for inline design, detailed in the flow-disturbing structures section. The design layouts of inline and staggered designs are illustrated in Fig. 1 (a–b).

Table 1
Structural properties of the cell.

Parameter	Value [m]
Radius of the cell (r_{batt})	1.05×10^{-2}
Radius of mandrel (r_{mand})	3×10^{-3}
Height of the cell (h_{batt})	7×10^{-2}
Cell casing thickness (d_{can})	2.5×10^{-4}

2.1. Battery thermal model

Designing an accurate heat generation model for a cell is vital for BTMS studies. Therefore, an electrochemical-thermal coupled model is used to uncover heat generation characteristics during discharge. Simplified models such as mapped heat release and equivalent circuit model yield an acceptable accuracy for the end of discharge with low accuracy in heat generation calculation during discharge. The electrochemical model of the cell comprises mass conservation, charge balance, heat generation and electrochemical kinetics equations, which were defined by Fuller, Doyle and Newman [44].

This model solves the electrochemical part of the cell in a 1D domain where ion flux occurs in the x-direction, whose equations and boundary conditions are explained in Appendix A. Battery thermal model is created by adopting the P3D method. In the P3D model, internal structure of the cell is treated as a single material, the thermodynamic properties of which are calculated by averaging all properties of cell materials as in Equations (6), (7), (14) and (15). In addition, heat generation is calculated as the average heat rate of active layers (anode, separator and cathode) of the cell, which is applied in the 3D model. Then, the volumetric average temperature of the 3D model is used as the temperature of the 1D model. The cell involves graphite anode, NCA cathode and $LiPF_6$ in 3:7 EC/EMC as electrolyte. Aluminum and copper are the materials of positive and negative current collectors, respectively. All the material properties are given in Appendix A.

2.2. Governing equations

The flow is designated as incompressible turbulent since the Reynolds number exceeded 4000 in the inlet region ($Re = \rho_{air} U_0 D_{hydraulic}/\mu_{air}$). The previous studies in the literature used k-ε turbulent model and it showed good compatibility with simulations and experiments [35,40,42]. Hence, k-ε turbulent model is adopted in this study. The governing equations for fluid flow are [45]:

$$\rho(\nabla \bullet U)\varepsilon = \nabla \bullet \left[\left(\mu + \frac{\mu_T}{\sigma_\varepsilon}\right)\nabla\varepsilon\right] + C_{\varepsilon 1}\frac{\varepsilon}{k}P_k - C_{\varepsilon 2}\rho\frac{\varepsilon^2}{k} \quad (1)$$

$$\rho(\nabla \bullet U)k = \nabla \bullet \left[\left(\mu + \frac{\mu_T}{\sigma_k}\right)\nabla \mathrm{k}\right] + P_k - \rho\varepsilon \quad (2)$$

ε and k are the dissipation rate and turbulent kinetic energy, respectively. The turbulent viscosity (μ_T) is calculated as in Equation (3) and the turbulence production (P_k) is calculated by Equation (4).

$$\mu_T = \rho C_\mu \frac{k^2}{\varepsilon} \quad (3)$$

$$P_k = \mu_T\left[\nabla U : \left(\nabla U + (\nabla U)^T\right) - \frac{2}{3}(\nabla \bullet U)^2\right] - \frac{2}{3}\rho k \nabla \bullet U \quad (4)$$

The boundary conditions (BCs) and initial conditions (ICs) of the problem are as follows:

- **Inlet:** The air enters to the flow domain with: $U_0 = 1.66\, m/s$ and $T_{in} = 20\,^{\circ}C$.
- **Outlet:** The temperature gradient in the flow direction and pressure are zero at the outlet surface.
- **Walls:** No-slip boundary condition imposed to all walls and top and bottom walls are adiabatic.
- **Initial conditions:** The temperature of the entire system is 20 °C at the initial time step.
- **Symmetry:** Symmetry boundary conditions were attained to the side surfaces, as shown in Fig. 1.

The model constants for turbulent flow are given in Table 2.
The energy balance of a cell is described as follows:

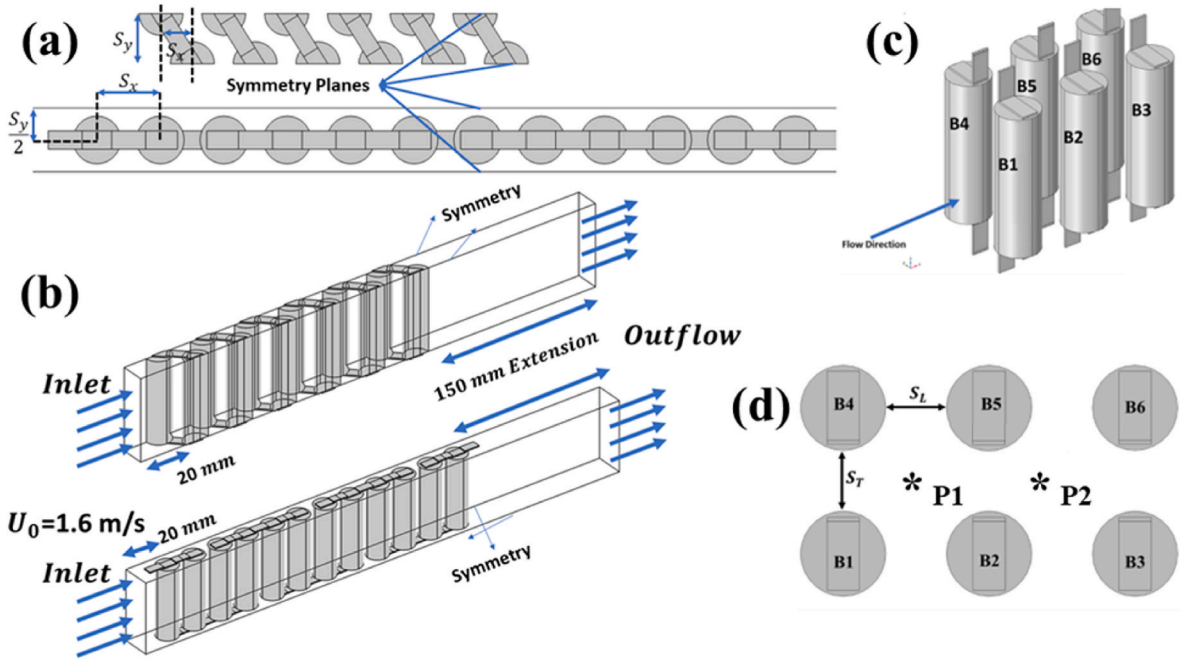

Fig. 1. Illustration of the module with 12 cells from the (a) top view and (b) 3D view. (c–d) Images of the distancing and how the cells are located in the simulation and experiment.

Table 2
Model constants of the turbulent flow model.

Constant	Value
C_μ	0.09
$C_{\varepsilon 1}$	1.44
$C_{\varepsilon 2}$	1.92
σ_ε	1.3
σ_k	1.0
U_0	1.66 m/s
p_0	0

$$\rho_{batt} Cp_{batt} \frac{\partial T}{\partial t} = \nabla(k \nabla T) + Q_{tot} \tag{5}$$

The parameter k is the thermal conductivity of the cell material (cf. Eq. (14) and (15)), where ∇T describes the temperature difference between the cell surface and the ambient. Moreover, ρ_{batt} and Cp_{batt} are the bulk properties of active material, which are calculated as follows:

$$Cp_{batt} = \frac{\sum_i L_i Cp_i}{L_{batt}} \tag{6}$$

$$\rho_{batt} = \frac{\sum_i L_i \rho_i}{L_{batt}} \tag{7}$$

The subscript i changes for current collectors, anode/cathode and separator. There are distinct sources of internal heat generation of a cell, which can be divided in parts as in Eq. (8):

$$Q_{tot} = Q_{rev} + Q_{irr} + Q_{ohm} \tag{8}$$

Reversible heat generation (Q_{rev}) stems from the potential change of electrode with temperature, also called entropic heat generation. Irreversible heat generation (Q_{irr}) occurs due to the over-potential demand of chemical reactions. Ohmic heat (Q_{ohm}) is generated due to the potential differences between solid and electrolyte domains. All heat generation terms are described in the following equations:

$$Q_{rev} = j^{Li+} T \frac{\partial E_{eq}}{\partial T} \tag{9}$$

$$Q_{irr} = j^{Li+} \left(\varphi_s - \varphi_l - E_{eq}\right) \tag{10}$$

$$Q_{ohm} = i_l \left(\frac{\partial \varphi_l}{\partial x}\right) + i_s \left(\frac{\partial \varphi_e}{\partial x}\right) \tag{11}$$

$$i_l = \left(\kappa^{eff} \frac{\partial \Phi_l}{\partial x} + \frac{2RT\kappa^{eff}}{F}\left(t_+^0 - 1\right)\left(1 + \frac{d \ln f_\pm}{d \ln c_l}\right) \frac{\partial \ln c_l}{\partial x}\right) \tag{12}$$

$$i_s = \sigma_s^{eff} \frac{\partial \Phi_s}{\partial x} \tag{13}$$

where i_s and i_l correspond to current density in solid and liquid phases, respectively. In addition, the thermal conductivity of the jelly roll (the active part that generates heat) is calculated as in Equations (14) and (15):

$$k_r = \frac{L_{batt}}{\sum_i \frac{L_i}{k_i}} \tag{14}$$

$$k_z = k_\theta = \frac{\sum_i L_i k_i}{L_{batt}} \tag{15}$$

The heat generation term is corrected as in Equation (16) before attaining it to the model. On the right-hand side of Equation (16), the first term describes the average heat generation of the anode, separator and cathode. Therefore, the second term represents the fraction of heat-generating layers and total cell length. The third term expresses the ratio between the jelly roll and the total cell volume.

$$Q_{tot,3D} = Q_{tot,1D} \frac{L_{neg} + L_{sep} + L_{pos}}{L_{batt} + L_{Al,cc} + L_{Cu,cc}} \frac{\left[(r_{batt} - d_{can})^2 - r_{mand}^2\right]\left[h_{batt} - 2d_{can}\right]}{\left[r_{batt}^2 - r_{mand}^2\right] h_{batt}} \tag{16}$$

2.3. Experimental setup

Two experiments are documented in this study to validate numerical simulations. Initially, a single cell was discharged with 0.1C, 1C, 3C and 5C by an electronic load (BK Precision 8614), where the cell was in natural convection condition with an ambient temperature of 20 ± 1 °C. Temperature (by K-type thermocouples) and voltage data were collected with a data logger (Hioki HiLOGGER LR8431). With the data of the single-cell experiment, a 1D electrochemical-thermal model of a cylindrical li-ion cell with NCA cathode, graphite anode and liquid electrolyte (Molicel 21700 INR P42A) was created by adopting some parameters from the literature and curve fitting several parameters based on the single-cell discharge data acquired from experiments.

Another experiment was carried out to validate the module level cooling simulation. First, a module was manufactured from plexiglass and three layers of honeycomb structures were placed to mimic the air manifold characteristics in the application. In the experiment, 120 mm × 120 mm AC fan supplied air to the 120 mm × 70 mm module. The experimental setup is shown in Fig. 2.

In Fig. 1(c–d), the distancing and how the batteries are located during the experiments can be seen. For experiments and the simulation, the distances between batteries are $S_T = S_L = 10$ mm. During the experiments, batteries were discharged with 3C for 1086 s, where the cut-off voltage is in accord with the supplier data, 2.5 V. The pack voltage and a single cell voltage were measured and recorded during the experiment. Temperature values were measured from the middle surface of batteries with K-type thermocouples. In addition, the inlet air temperature was also measured during the experiments and it was 20 ± 0.5 °C.

2.4. Numerical simulations

All numerical solutions were simulated by COMSOL Multiphysics 5.5. The convergence criterion of turbulent flow is 10^{-4} and those of battery simulation and heat transfer are 10^{-5} and 10^{-6}, respectively. During the pack level simulations, turbulent flow and heat transfer modules are coupled with 1D lithium-ion battery module in COMSOL Multiphysics 5.5. Electrochemical and thermal models were simulated in a time-dependent manner, whereas fluid flow was solved as a steady-state due to time-independent characteristics of the fluid flow in the considered conditions [46].

The single-cell simulation is used to validate the battery thermal model which includes a cylindrical cell with busbars. While solving the single-cell model, 6 $\frac{W}{m^2 K}$ heat transfer coefficient is attained to the cell surface, which is an approximated value for natural convection [47]. The time step is taken as 1 s while solving heat transfer and battery models with a segregated solver, which solves the battery equations given in Appendix A firstly and energy equations secondly.

The experimental setup and the numerical simulations have the same dimensions. Six cells are in the middle of the cooling channel which is 120 mm in width and 70 mm in height. The inlet and outlet ports of the model are extended by 20 mm and 150 mm, respectively, to acquire developed flow characteristics during the solution. Lastly, all heat transfer enhancements are performed on a module level simulation consisting of 12 cells connected in a 2P6S arrangement. These enhancements involve changing cell-to-cell distances and the addition of spoilers.

For the spoilers, cylindrical structures with various dimensions are inserted between half of the cells in the module. Cylindrical spoilers were chosen as they mildly change the flow direction like the staggered

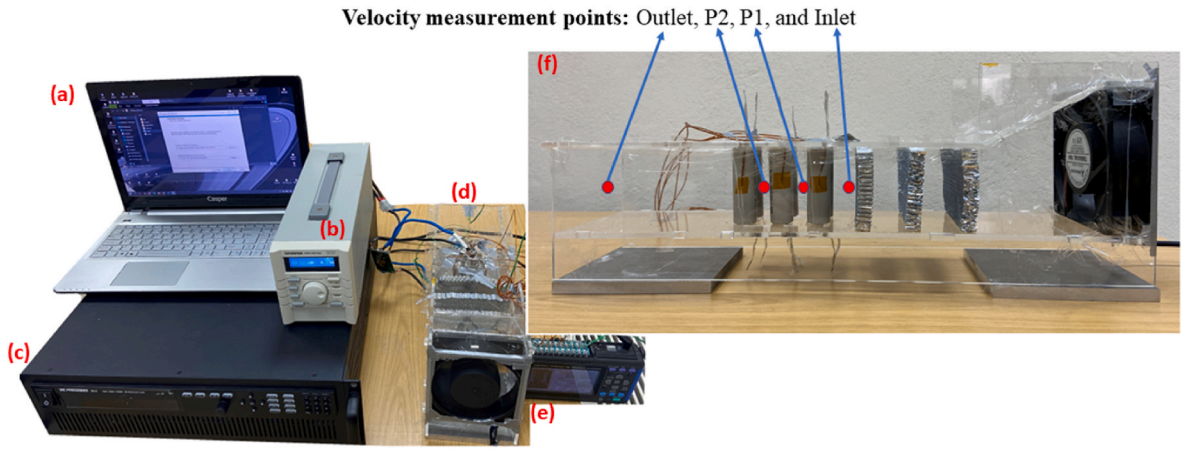

Fig. 2. (a) Computer for data interpretation, (b) power supply (GW Instek PSH 2018a), (c) electric load (BK Precision 8614), (d) the module with fan, (e) data acquisition centre (Hioki HiLOGGER LR8431), (f) the module side view without connections.

design. However, unlike staggered designs, cylindrical spoilers were thinner than the cells and placed in an anti-symmetrical pattern to focus on improving airflow near the hot spots. Then, diamond and triangle-shaped spoilers that fit into the largest cylinder are inserted to find out how unused air regions can be diminished. Delta winglets are used since they were the most effective ones in the literature [48]. In addition, the centroid of cylindrical, triangular and diamond-shaped spoilers is located equidistantly from adjacent cells, but winglet positions are adapted from Lemouedda's study [49]. In Fig. 3, spoiler shapes and their locations are illustrated. To save computational cost, symmetry boundary conditions were employed. These simulations conducted for several alignments, spacings and flow-disturbing structures, results of which are documented in the results section.

All designs illustrated above involve 12 cells in total and the inlet velocity of air was 1.66 m/s. The volumetric power densities were calculated to compare the efficiency of each design, calculated as in Equation (17), where N_{batt} represents the number of batteries. In addition, the heat transfer performance coefficient, adopted from Ghobadi's study [50], was used to have a clear understanding of the heat transfer enhancement and pressure drop variation of each design, which is given in Equation (18):

$$P_{Vol} = \frac{12 \times 4.2}{S_y \times h_{batt} \times (N_{batt} - 1) \times S_x} \tag{17}$$

$$\frac{Nu_b/Nu}{\left(f_b/f\right)^{1/3}} \tag{18}$$

3. Results and discussion

Simulation results and validation processes are documented in this section. In addition, the cooling performance of various designs for lithium-ion battery modules with 12 cells is documented and compared. The module discharge rate is 3C and design improvements were made by changing cell-to-cell distances and inserting spoilers. To understand the effect of spoilers on thermal efficiency, first, the module level simulations were conducted for several cell distances without baffles. Then, several cylindrical structures with 6 mm diameter were inserted between the cells, especially near those with relatively higher average temperatures. There are several sizes of cylindrical baffles and the most

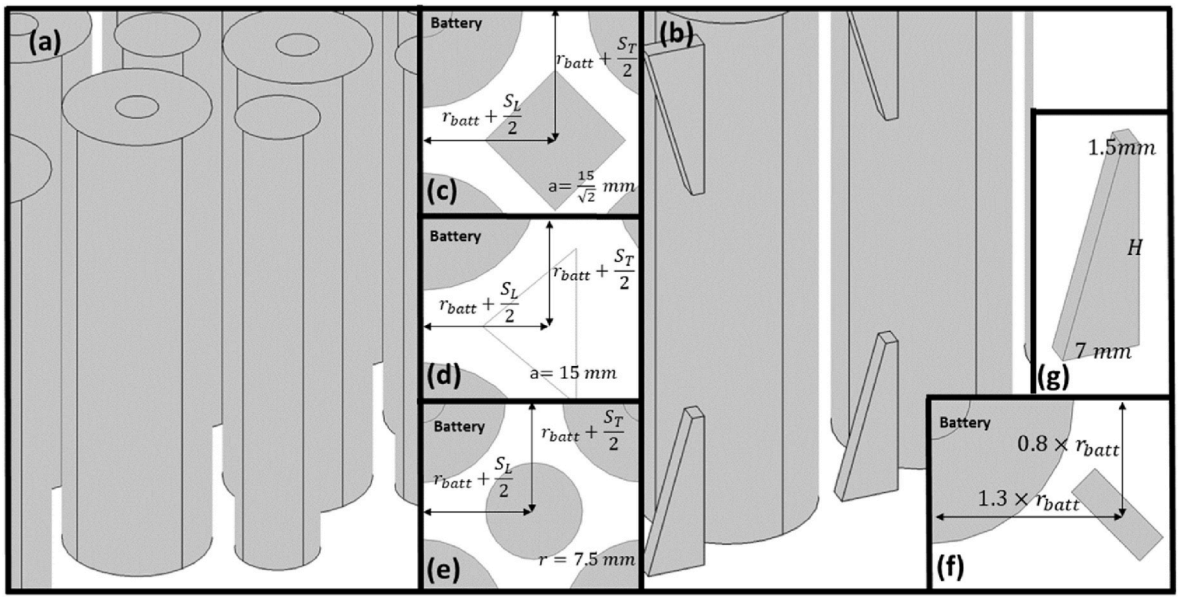

Fig. 3. The illustration of (a) cylindrical spoilers and (b) winglets in 3D view. Placements of (c) diamond, (d) triangular, (e) cylindrical and (f) winglet type spoilers from top view. (g) Dimensions of winglet structure.

effective one is the spoiler with a 15 mm diameter. Therefore, escribed circle diameters of triangular and diamond-shaped spoilers were set to 15 mm as well. Furthermore, winglets are symmetrically located on the top and bottom walls and their lengths and angles were varied to find the best option. The range for angles were 15°–75° and winglet lengths were varied between 10 mm and 35 mm.

3.1. Experimental and numerical validation

As expressed in Appendix A, several battery parameters were curve fitted in order to supply the required data to the battery model. For this reason, a single-cell experiment and its simulation were used to validate the battery thermal model. The single-cell model was simulated with COMSOL Multiphysics 5.5 and subjected to a mesh refinement study between 10×10^3 and 300×10^3 elements. However, since there was no significant dependency on a mesh structure, a mesh structure with 48000 elements was used.

The cell was discharged with 0.1C, 1C, 3C and 5C in numerical simulations as well as experiments. In numerical studies, average surface temperature of the cell was compared with the average temperature of three distinct points in experiments (top, middle and bottom). Fig. 4 documents the temperature and voltage curves of various C-rates for both numerical simulations and experiments. It can be seen from the figure that the discrepancies between simulation and experiments increase as the discharge rate increases. While the maximum temperature and voltage differences between the simulation and experiment are 3.14 °C and 0.25 V for the 3C discharge rate, they become 5.6 °C and 0.6 V for 5C.

The channel dimensions where the cells are located are identical in module level simulations and experiments. First, a mesh independency test was conducted by varying the mesh sizes to uncover how many numbers of mesh elements are required for mesh-independent simulation results. The deviation of the results for various mesh element sizes are given in Table 3.

According to the results of grid independency, Table 3, 3.7×10^5 elements were used in simulations, as it yields acceptable relative error with the minimum number of mesh elements. The pack was discharged with 3C (25.2 A) for 1120 s. Temperature and voltage curves of simulations showed a similar trend with experiments with a few fluctuations. Fig. 5 demonstrates the pack voltage and surface temperature curves of both module level simulation and experiment. Furthermore, the air velocity was measured at several points in experiments by a hot wire anemometer (Testo 435). Its probe was kept at specific points for 1 min to measure time-averaged velocities. The velocity comparisons between the simulation and experiment are given in Table 4.

The results show that the battery model and flow simulation are viable for pack simulations. For this reason, the cooling performance of battery packs will be investigated and enhanced for the rest of this study. In addition, another mesh refinement study was conducted for the module with 12 cells and it is tabulated in Table 5. Since its errors were acceptable, the mesh structure around 7×10^5 elements was used.

Table 3
Effect of the number of mesh elements on surface temperatures.

Number of elements	$T_{average,1}$ °C	$T_{average,2}$ °C	$T_{average,3}$ °C	$T_{average,4}$ °C	$T_{average,5}$ °C	$T_{average,6}$ °C
158936	37.685	40.875	41.290	37.717	40.801	41.283
217448	36.881	40.138	40.946	36.906	40.053	40.919
304627	36.754	40.391	41.021	36.794	40.330	40.994
371380	37.193	40.237	40.634	37.175	40.245	40.597
1148084	37.248	40.118	40.516	37.252	40.123	40.492
Number of elements	$Error_T$ %	$Error_T$ %	$Error_T$ %	$Error_T$ %	$Error_T$ %	$Error_T$ %
158936	–	–	–	–	–	–
217448	2.13	1.80	0.83	2.15	1.83	0.88
304627	0.344	0.63	0.18	0.30	0.69	0.18
371380	1.19	0.38	0.94	1.03	0.21	0.96
1148084	0.148	0.294	0.29	0.20	0.30	0.26

3.2. Experimental accuracy and reproducibility

Experiments were conducted to observe how air temperature and discharge rate affect the results. Furthermore, 3C discharge case and the base case were repeated three times on distinct days to understand the experimental accuracy and reproducibility of experiments. Experimental and simulated cases are entitled as Ex1-5 and Sim1-3, respectively. Ex1 to Ex3 represent the repetition experiments in distinct days with 3C at 20 °C and Ex4 and Ex5 stand for 3C discharge rate at 25 °C inlet temperature and 1C discharge rate at 20 °C temperature, respectively.

All the cases mentioned above were compared with simulations of the same variables. The comparison was made by calculating mean absolute errors between simulations and experiments, cf. Equation (19). In addition, Ex1-3 were compared with each other. Since six distinct temperature data were collected from batteries, the errors associated with them were calculated individually. The arithmetic mean of these values was used to acquire an overall understanding.

$$\overline{\delta} = \frac{\sum_{1}^{N} \frac{|T_{sim} - T_{exp}|}{T_{exp}} \times 100}{N} \tag{19a}$$

Table 6 documents the mean absolute error between experiments and simulations. According to the table, the maximum error for

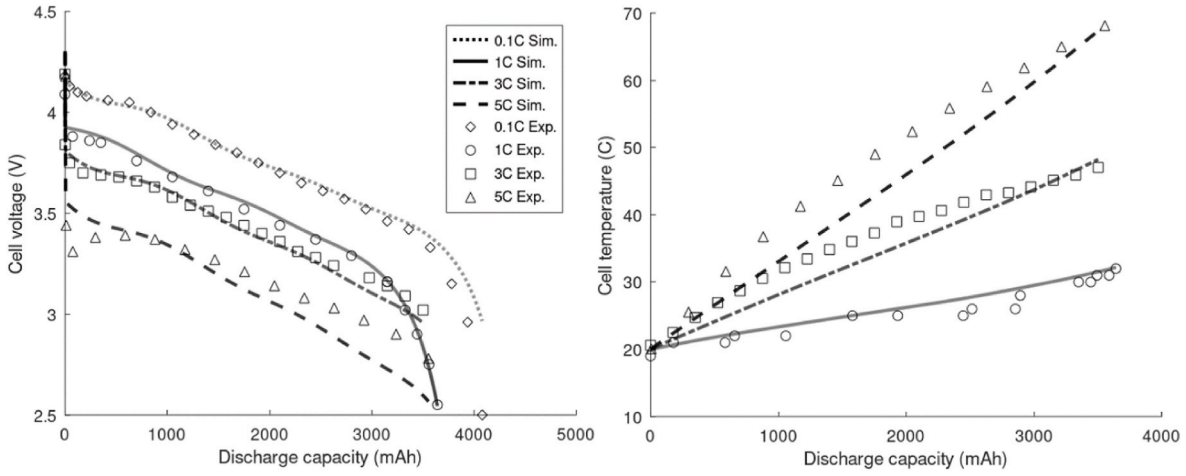

Fig. 4. The comparison of experimental and simulation temperatures and voltages for the single-cell model.

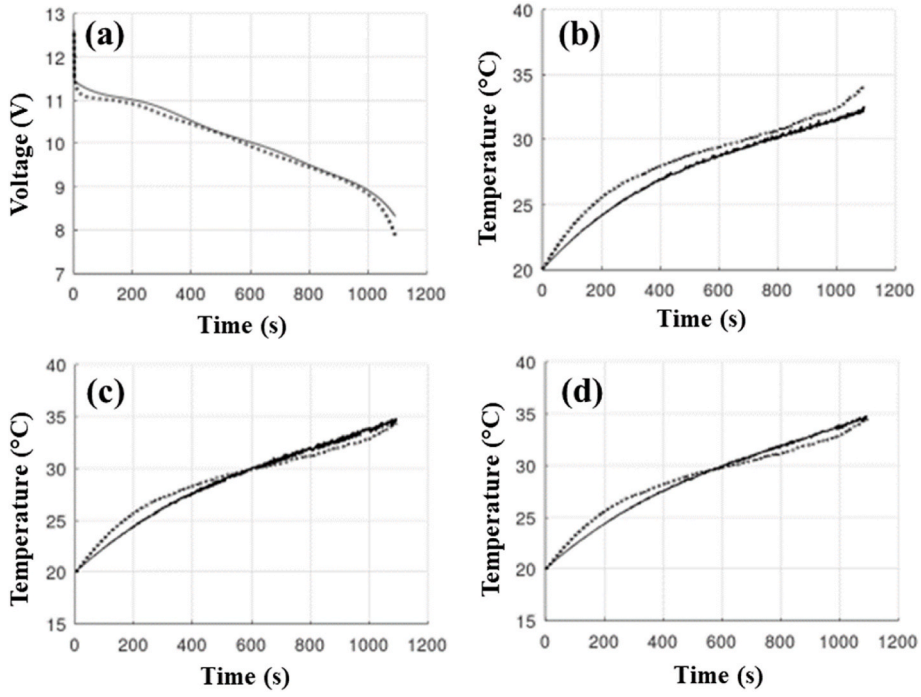

Fig. 5. Voltage (a) and temperature curves of B4(b), B5(c) and B6(d) in module-level simulation(solid) and experiment(dotted).

Table 4
Velocity measurements of simulation and experiment.

Measuring point	Simulation (m/s)	Experiment (m/s)
Inlet	1.629	1.65
Outlet	1.63	1.61
P1 (Fig. 1(d))	3.55	3.83
P2 (Fig. 1(d))	3.2	3.58

Table 5
Grid independence of battery module with 12 cells.

Number of elements	$T_{average,1}$	$T_{average,7}$	$T_{average,12}$	$T_{average,outlet}$
	°C	°C	°C	°C
632410	34.190	36.206	38.256	32.502
704124	34.182	36.411	38.291	32.442
1021844	34.366	36.283	38.344	32.470
1337197	34.366	36.283	38.344	32.477
Number of elements	$Error_T$	$Error_T$	$Error_T$	$Error_T$
	%	%	%	%
632410	–	–	–	–
704124	0.022	0.567	0.092	0.181
1021844	0.538	0.351	0.138	0.085
1337197	0	0	0	0.021

Table 6
Errors between experiments and simulations.

Cases	Error	Cases	Error
$\delta_{Ex1-Ex2}$	1.3%	$\delta_{Ex2-Sim1}$	6.42%
$\delta_{Ex1-Ex3}$	5.9%	$\delta_{Ex3-Sim1}$	3.1%
$\delta_{Ex2-Ex3}$	7.45%	$\delta_{Ex4-Sim2}$	2.26%
$\delta_{Ex1-Sim1}$	5.3%	$\delta_{Ex5-Sim3}$	1.47%

experiment-to-experiment comparisons is 7.5%. That is caused by fluctuations (2 °C) in the ambient conditions where the experiment was conducted. Measurement errors also cause this divergence between identical experiments. Since this study mainly focuses on thermal management improvements, theoretical and experimental values following the same trend with an accuracy of >90% are considered to be adequate to ensure the reliability of the model. As mentioned in the experimental and numerical validation section, the error between the simulation and experiment increases as the discharge rate increases. Therefore, the error between the experiment and simulation is the lowest at 1C, given in Table 6.

3.3. Cell distances

Cell-to-cell distances (δ_{cell}) were investigated for both staggered and inline layouts. As the distance between cells increases, temperature uniformity improves, but it does not affect the maximum temperature significantly, as shown in Table 7. Even though spacious design contains more volume flow rate than congested designs, they cannot provide better cooling because of unused air regions.

The temperature contours are generated from the cross-section plane

Table 7
Outcomes of various designs.

Design	P_{fan} (W)	T_{max} (°C)	ΔT_{max} (°C)	Power density
$S_x = S_y = 28\ mm$ $\delta_{cell} = 7\ mm$	0.27	38.3	4.12	281 W/l
$S_x = S_y = 36\ mm$ $\delta_{cell} = 15\ mm$	0.095	38.2	2.54	172 W/l
Staggered $\delta_{cell} = 7\ mm$	0.23	35.51	2.7	328 W/l
Cylinder D = 6 mm	0.44	38.03	3.8	
Cylinder D = 9 mm	0.54	37.78	3.6	
Cylinder D = 15 mm	0.89	37.14	2.92	
Square	0.82	36.91	2.75	
Triangle	0.98	36.6	2.5	
Winglet 10 mm	0.33	38.2	3.98	
Winglet 15 mm	0.37	37.8	3.6	
Winglet 20 mm	0.39	37.7	3.5	
Winglet 26 mm	0.45	37.8	3.6	
Winglet 35 mm	0.46	38.75	4.53	

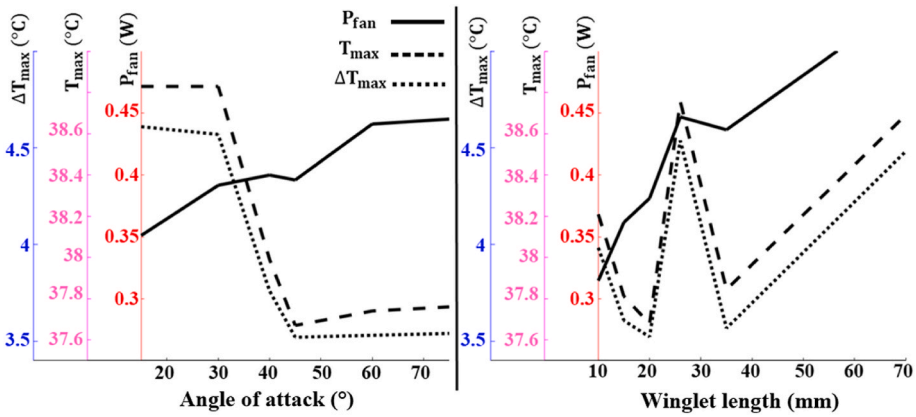

Fig. 6. Maximum temperature and temperature difference and parasitic power consumption changes over the angle of attack and length of delta winglet design.

located 35 mm above the battery tabs. It can be interpreted from this section that air cooling mechanisms require improvements that increase the heat transfer coefficient between the cells and air. Many unused cold air regions can be found even in the 7 mm designs. Since this cold air leaves the cooling channel without absorbing heat, those designs have the potential for cooling improvement by mixing the coolant.

3.4. Flow-disturbing structures

Mixing the airflow with spoiler structures is an option for increasing the contribution of unused air regions. According to the simulation results, the average temperature of the air after the sixth cell is greater than the entrance as expected due to the thermal boundary layer thickness increment. The heat transfer can be increased by changing the flow characteristics after the sixth cell. For this purpose, cylindrical blocks were placed between adjacent cells, as shown in Fig. 3. Based on Table 7, since cylindrical spoilers of 15 mm diameter yielded the best results regarding the temperature profile, other shapes were fitted inside a 15 mm cylinder, as detailed in Fig. 3.

3.5. The effect of winglets

Winglet design optimizations were conducted based on the angle of attack and winglet height. Since equal sizes of winglets were placed on both walls, their height could not exceed 35 mm, which corresponds to half of a cell. However, 70 mm winglets were placed on only one side for observation. Fig. 6 shows how winglet length and angle of attack affect the fan power consumption (calculated by Eq. (19)), maximum temperature and temperature gradient.

$$P_{fan} = U_0 \times h_{batt} \times S_y \times (P_{in} - P_{out}) \quad (19)b$$

The efficiency of various heights was evaluated for the optimum angle (45°). The right-hand side graph in Fig. 6 shows that power consumption gradually increases as winglet height increases. Therefore, according to the results, the optimum winglet has 20 mm height and 45° angle of attack which minimizes the maximum temperature and

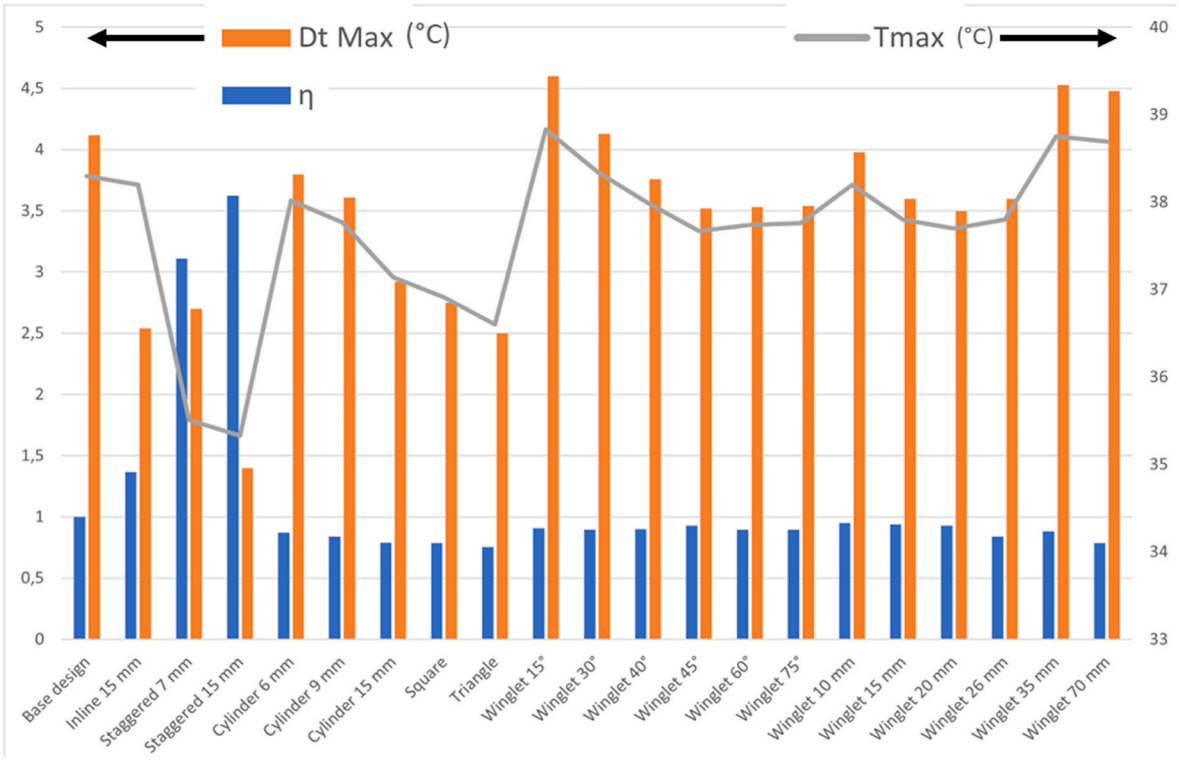

Fig. 7. Heat transfer performance coefficients, maximum temperature differences and peak temperature comparisons of all designs.

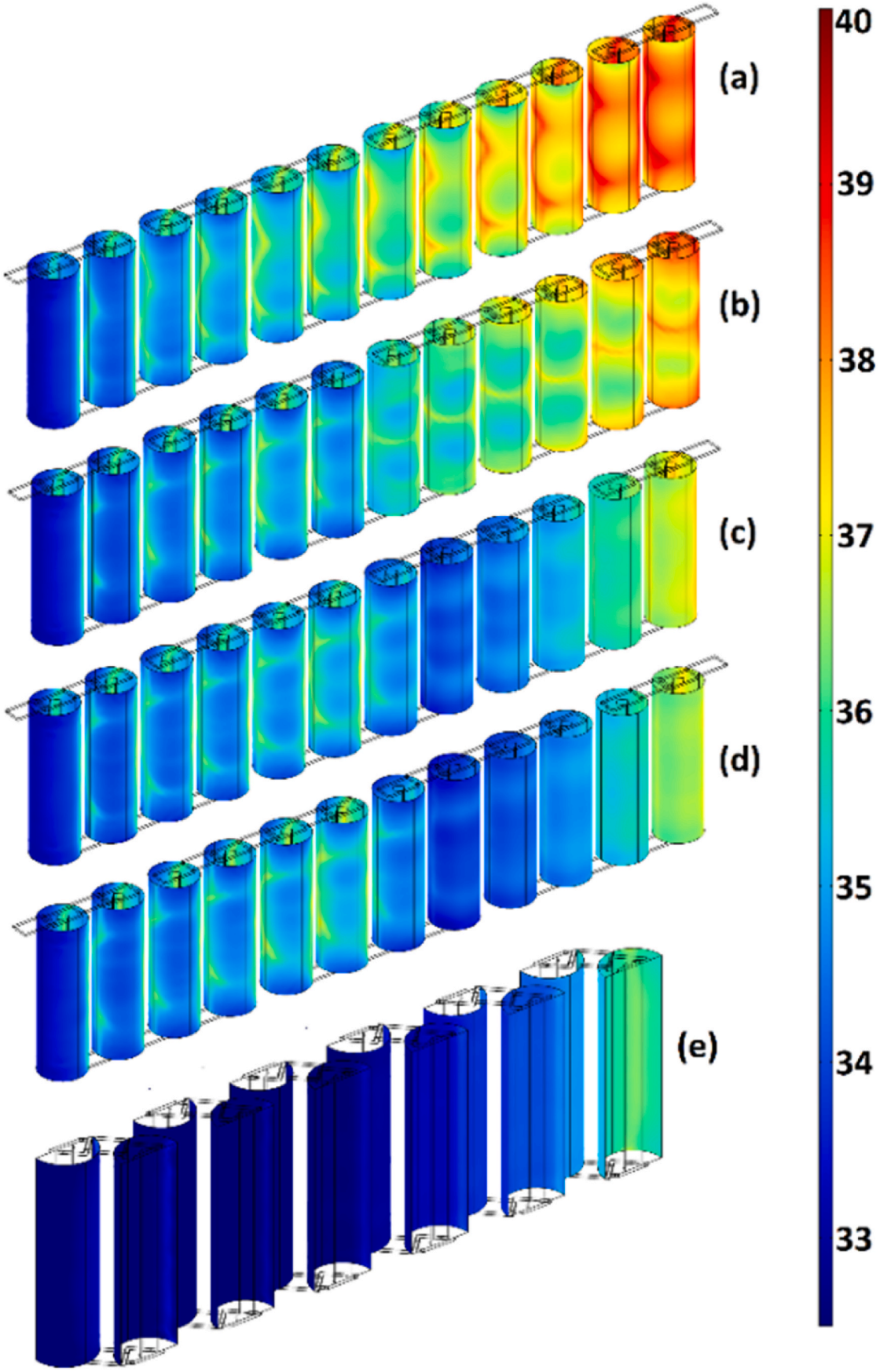

Fig. 8. Temperature (in °C) profiles of (a) inline alignment without spoiler (base), (b) winglet (optimum), (c) diamond, (d) triangular and (e) staggered alignment designs.

maximum temperature difference with minimum parasitic power consumption.

3.6. Overall thermal performance

Each design can be compared clearly by adopting a performance parameter used in the heat exchanger literature. Ghobadi et al. [50] documents a performance parameter involving the Nusselt number and fanning friction factors, given in Equation (18).

While Nu_b and f_b describe the Nusselt number and friction factor of baffled designs, variables without subscripts stand for the base design. In this study, the average heat transfer coefficient was inserted instead of the Nusselt number and pressure drops were used instead of the friction factor. The performance of all enhancements was compared with the base design (inline alignment and $\delta_{cell} = 7$ mm). In Fig. 7, maximum temperature, maximum temperature difference and heat transfer performance parameters of each design are given. Based on the graph, even though triangular baffles yield one of the best results in terms of temperature and temperature difference, the heat transfer performance of the triangular design is relatively low due to the high pressure drop associated with the design.

On the other hand, winglet design layouts offer moderate cooling with heat transfer parameters closer to the base design than the triangular layout. Staggered battery alignment provides the best cooling performance with the lowest peak temperature and temperature difference. Table 7 documents cooling performance and fan power consumption of the optimal designs. Triangle spoilers yielded the best cooling performance with a significant increase in parasitic power, which was 0.72 W higher than the base design.

Furthermore, square and 15 mm cylinders offer a moderate cooling option. In addition, delta winglet vortex generators yielded efficient cooling performance with negligible surplus power consumption. Staggered battery packs offer the highest volumetric power density with better cooling performance than the inline alignment, as shown in Table 7. It offers 10% better cooling than the best design of the inline alignment. Volumetric power density of the staggered pack is 328 W/l, approximately 17% better than the inline alignment. In addition, fan power consumption of the staggered design is relatively low (0.33 W). Fig. 8 documents the surface temperature profiles at the last step of the aforementioned optimal designs.

4. Conclusion

This work highlights the cooling improvement of air-cooled battery modules with additional flow-disturbing structures by conducting numerical studies validated via experiments. The simulation was conducted with 3D heat transfer and turbulent flow simulations coupled with a 1D multiscale electrochemical battery model for 21700 cylindrical lithium-ion cells. Several experiments were performed to confirm the accuracy of the battery and air-cooling models, with the errors varying between 3% and 7%. Batteries were discharged under a 3C rate while being cooled down by airflow of 1.66 m/s velocity and 20 °C temperature. Spoilers were located in the module without changing cell-to-cell distances to compare the effect of spoilers. Mainly four types of spoilers; cylindric, triangular, diamond and delta winglet vortex generators were used. In addition, fan power consumptions, maximum cell temperatures and temperature gradients were documented for each case. The analyses yield to following results:

(i) As cell distances increase, the temperature gradient improves by 38% (2.6 °C), but the maximum temperature is not affected because of stagnant air regions in the cooling channel.
(ii) The cooling performance can be improved by inserting spoilers (the maximum temperature and temperature gradient are reduced up to 5% and 40%, respectively), which mixes the air and increases the heat transfer coefficient between the battery and air. Since spoiler structures can double the fan power consumption, careful optimizations are required for applications.
(iii) Delta winglet vortex generators effectively improve cooling by increasing power consumption by 40% (0.12 W). Winglet designs are the optimal solution for cooling efficiency, but they suffer from the increased parasitic power consumption.
(iv) Staggered layouts are superior to inline arrangements as their positions lead to wavy airflow formation, which reduces the maximum temperature by 7% (2.8 °C) and temperature gradient by 35% (1.4 °C). Also, since the flow path does not change aggressively, the pressure drop of the staggered design is 15% lower than the base design.

CRediT authorship contribution statement

R. Cagtay Sahin: Conceptualization, Methodology, Validation, Formal analysis, Investigation, Visualization, Writing – original draft. **Sinan Gocmen:** Methodology, Validation, Investigation, Writing – review & editing. **Erdal Cetkin:** Supervision, Conceptualization, Methodology, Writing – review & editing.

Declaration of competing interest

The authors declare that they have no known competing financial interests or personal relationships that could have appeared to influence the work reported in this paper.

Data availability

Data will be made available on request.

APPENDIX A

In the multiscale battery model, lithium ions are transferred in 1D, the path between two electrodes, since there is a significant length scale difference between other directions [51]. However, the phase change of ions between the solid and liquid states is defined in the 2D spherical domain and ion transfer occurs in a porous medium.

$$\frac{\partial c_s}{\partial t} = \frac{D_s}{r^2}\frac{\partial}{\partial r}\left(r^2\frac{\partial c_s}{\partial r}\right) \tag{A.1}$$

Equation A.1 defines the solid-state mass transfer in porous electrodes. The boundary conditions are given in Equations A.2 and A.3: $\frac{\partial c_s}{\partial r}\Big|_{r=0} = 0$ (A.2)

$$\left.\frac{\partial c_s}{\partial r}\right|_{r=r_p} = \frac{j^{Li+}}{a_s F} \tag{A.3}$$

where a_s stands for effective surface area, which is:

$$a_s = \frac{3\varepsilon_s}{r_p} \tag{A.4}$$

The phase change occurs on the surface of spherical particles as much as the current density (j^{Li+}). Liquid-state ion transfer is defined by Equation A.5 with the boundary conditions Equations A.6-A.11:

$$\frac{\partial \varepsilon_l c_l}{\partial t} = \frac{\partial}{\partial x}\left(D_l^{eff}\frac{\partial c_l}{\partial x}\right) + \frac{1 - t_+^0}{F} j^{Li+} \tag{A.5}$$

Equations A.6 and A.7 are called no-flux boundary conditions since current collectors do not contain ions. Equations A.8-A.11 define electrode-separator interfaces [52].

$$\left.\frac{\partial c_l}{\partial x}\right|_{x=0} = 0 \tag{A.6}$$

$$\left.\frac{\partial c_l}{\partial x}\right|_{x=L_{batt}} = 0 \tag{A.7}$$

$$\varepsilon_l \left(\frac{\partial c_l}{\partial x}\right)\Big|_{x=L_{neg}} = \varepsilon_{l,sep}\left(\frac{\partial c_l}{\partial x}\right)\Big|_{x=L_{neg}} \tag{A.8}$$

$$\varepsilon_l \left(\frac{\partial c_l}{\partial x}\right)\Big|_{x=L_{neg}+L_{sep}} = \varepsilon_{l,sep}\left(\frac{\partial c_l}{\partial x}\right)\Big|_{x=L_{neg}+L_{sep}} \tag{A.9}$$

$$c_l\left(L_{neg}\ , t\right) = c_{l,sep}\left(L_{neg}\ , t\right) \tag{A.10}$$

$$c_{l,sep}\left(L_{neg} + L_{sep}\ , t\right) = c_l\left(L_{neg} + L_{sep}\ , t\right) \tag{A.11}$$

Also, there are charge balance equations identifying the balance between the number of lithium ions transferred and the amount of charge transfer, coupled with mass transfer equations and electrochemical kinetics equations. The potential in the solid phase is defined with Ohm's law, which is given in Equation A.12 with its boundary conditions in Equations A.13-A.16:

$$\frac{\partial}{\partial x}\left(\sigma_s^{eff}\frac{\partial \Phi_s}{\partial x}\right) = j^{Li+} \tag{A.12}$$

$$\sigma_s^{eff}\frac{\partial \Phi_s}{\partial x}\Big|_{x=L_{batt}} = -I_{app} \tag{A.13}$$

$$\sigma_s^{eff}\frac{\partial \Phi_s}{\partial x}\Big|_{x=L_{neg}+L_{sep}} = 0 \tag{A.14}$$

$$\sigma_s^{eff}\frac{\partial \Phi_s}{\partial x}\Big|_{x=L_{neg}} = 0 \tag{A.15}$$

$$\Phi_s|_{x=0} = 0 \tag{A.16}$$

The charge balance in the liquid phase is expressed in Equation A.17 and its boundary conditions are defined in Equations A.18-A.21:

$$\frac{\partial}{\partial x}\left(\kappa^{eff}\frac{\partial \Phi_l}{\partial x}\right) + \frac{\partial}{\partial x}\left(\frac{2RT\kappa^{eff}}{F}\left(t_+^0 - 1\right)\left(1 + \frac{d\ln f_{\pm}}{d\ln c_l}\right)\frac{\partial \ln c_l}{\partial x}\right) = -j^{Li+} \tag{A.17}$$

$$\left.\frac{\partial \Phi_l}{\partial x}\right|_{x=0} = 0 \tag{A.18}$$

$$\left.\frac{\partial \Phi_s}{\partial x}\right|_{x=L_{batt}} = 0 \tag{A.19}$$

$$\Phi_l\left(L_{neg}\ , t\right) = \Phi_l\left(L_{neg}\ , t\right) \tag{A.20}$$

$$\Phi_l\left(L_{neg} + L_{sep}\ , t\right) = \Phi_l\left(L_{neg} + L_{sep}\ , t\right) \tag{A.21}$$

The Butler-Volmer equation describes the relationship between the total current and potentials, which is given in Equation A.22.

$$j^{Li+} = a_s i_0\left[exp\left(\frac{\alpha_a F}{RT}\eta\right) - exp\left(-\frac{\alpha_c F}{RT}\eta\right)\right] \tag{A.22}$$

The equivalent voltage for the cathode is a polynomial, the parameters of which were fitted with the polynomial regression method based on the 0.1C discharge curve and anode equivalent voltage curve from the literature [53]. Cathode voltage polynomial coefficients are given in Table A1 and equivalent voltage functions are given in Equations A.23 and A.24.

$$E_{eq,pos} = \sum_{i=0}^{22} A_i x^i \tag{A.23}$$

$$E_{eq,neg} = 0.6379 + 0.5416\ exp(-305.5309 \times y) + 0.044 \tanh\left(-\frac{y - 0.1958}{0.1088}\right) - 0.1978 \tanh\left(\frac{y - 1.0571}{0.0854}\right) - 0.6875 \tanh\left(\frac{y + 0.0117}{0.0529}\right) - 0.0175 \tanh\left(\frac{y - 0.5692}{0.0875}\right) \tag{A.24}$$

Table A.1
Polynomial coefficients for cathode equivalent voltage.

Parameter	Value	Parameter	Value	Parameter	Value
A_0	*398.01336013198392*	A_8	*496823.58244024246*	A_{16}	*31493.18267972166*
A_1	*−6296.1076950394308*	A_9	*−421106.34179412422*	A_{17}	*−1084234.1893559622*
A_2	*41959.219071580315*	A_{10}	*354200.00761110592*	A_{18}	*92159.424582747262*
A_3	*−147857.02171270244*	A_{11}	*−490432.27097464772*	A_{19}	*819007.96409683058*
A_4	*287870.02690709516*	A_{12}	*356826.47806278308*	A_{20}	*197218.48943382909*
A_5	*−295327.71817991912*	A_{13}	*−295625.16819127946*	A_{21}	*−778437.66013222793*
A_6	*180105.05120692172*	A_{14}	*138640.00521595744*	A_{22}	*285035.16062089079*
A_7	*−271903.1222659052*	A_{15}	*509484.82719697087*		

Material properties of the cell are given in Table A2. Equations A.25-A.27 define the solid-state diffusion coefficient of the cathode, liquid-state diffusion and liquid-state electronic conductivity, respectively [51].

Table A.2
Battery parameters.

Parameter	Anode	Separator	Cathode	CC Neg.	CC Pos.	Ref.
Length (μm)	17	16	13	15	10	*
ε_l	0.3825	0.47	0.3382	–	–	[51]
ε_s	0.5802	–	0.4483	–	–	[51]
α_a & α_c	0.5	–	0.5	–	–	[51]
$c_s^{max}\ (mol/m^3)$	28200	–	49195	–	–	[51]
$c_s^0\ (mol/m^3)$	$0.65 \times c_s^{max}$	–	$0.41 \times c_s^{max}$	–	–	[54]
σ_s & $\sigma_l\ (S/m)$	16700	cf. Eq. (A.27)	0.04	–	–	[51]
D_s & $D_l\ (m^2/s)$	1×10^{-3}	cf. Eq. (A.26)	cf. Eq. (A.25)	–	–	[51]
$\rho\ (kg/m^3)$	2500	1200	3000	–	–	[51]
$C_p\ (J/kg/K)$	800	800	1000	385	875	[51,55]
$k\ (W/m/K)$	1.04	1	2	398	200	[51,55]
c_l^0	1150	1150	1150	–	–	*
c_l^{ref}	1000	–	1000	–	–	*

*Fitted parameters based on the single-cell experiment.

$$D_{s,pos} = \frac{3.3 \times 10^{-13}}{(x - 0.02)^2} \tag{A.25}$$

$$D_l = 10^{-\left(4.43 + \left(\frac{54}{\left(T - \left(229 + 5\left(\frac{c_l}{1000}\right)\right)\right)}\right) + 0.22\frac{c_l}{1000}\right)} \times 10^{-4} \tag{A.26}$$

$$\sigma_l = \left(-8.2488 + 0.053248T - 2.9871 \times 10^{\left(-5T^2\right)} + 0.26235\left(\frac{c_l}{1000}\right) - 9.3063 \times 10^{\left(-3\frac{c_l}{1000}T\right)} + 8.069 \times 10^{\left(-6\frac{c_l}{1000}T^2\right)} + 0.22002\left(\frac{c_l}{1000}\right)^2 - 1.765 \times 10^{\left(-4\left(\frac{c_l}{1000}\right)^2 T\right)}\right)^2 \left(\frac{c_l}{10000}\right) \tag{A.27}$$

The active layer thicknesses and reaction rates (i_0) were changed based on the experimental data by adjusting them for battery capacity and overpotential heat generation under different C-rates. Reaction rates and polynomial coefficient changes based on the discharge rate are listed in Table A3.

Table A.3
Reaction rates for anode and cathode.

C-rate	Anode	Cathode	A_0
0.1	0.5	3	A_0
1	0.015	0.07	A_0 +0.2583
3	0.0063	0.013	A_0 +0.2771
5	0.0008	0.0008	A_0 +0.3211

References

[1] R. Nealer, D. Reichmuth, D. Anair, Cleaner Cars from Cradle to Grave, Union Concerned Sci., 2015, pp. 1–54 [Online]. Available: http://www.ucsusa.org/sites/default/files/attach/2015/11/Cleaner-Cars-from-Cradle-to-Grave-exec-summary.pdf.

[2] M. Wicki, G. Brückmann, F. Quoss, T. Bernauer, What do we really know about the acceptance of battery electric vehicles?–Turns out, not much, Transport Rev. (2022) 1–26, https://doi.org/10.1080/01441647.2021.2023693.

[3] A. Pesaran, Battery thermal management in EVs and HEVs : issues and solutions, *Adv. Automot. Batter. Conf.*, no. January 2001 10 (2001).

[4] M. Morris, Comparison of rechargeable battery technologies, ASME Early Career Tech. J. 11 (November 2012) (2012) 148–155.

[5] M. Armand, Nature lithium battery, Nature 414 (November) (2001) 359–367 [Online]. Available: http://www.ncbi.nlm.nih.gov/pubmed/11713543.

[6] S. Ma, et al., Temperature effect and thermal impact in lithium-ion batteries: a review, Prog. Nat. Sci. Mater. Int. 28 (6) (2018) 653–666, https://doi.org/10.1016/j.pnsc.2018.11.002.

[7] H. Cavers, P. Molaiyan, M. Abdollahifar, U. Lassi, A. Kwade, Perspectives on improving the safety and sustainability of high voltage lithium-ion batteries through the electrolyte and separator region, Adv. Energy Mater. 12 (23) (2022), https://doi.org/10.1002/aenm.202200147.

[8] L. Su, E. Jo, A. Manthiram, Protection of cobalt-free LiNiO2from degradation with localized saturated electrolytes in lithium-metal batteries, ACS Energy Lett. 7 (6) (2022) 2165–2172, https://doi.org/10.1021/acsenergylett.2c01081.

[9] F. Elizalde, et al., Self-healable dynamic poly(urea-urethane) gel electrolyte for lithium batteries, J. Mater. Chem. 10 (23) (2022) 12588–12596, https://doi.org/10.1039/d2ta02239g.

[10] N.N.M. Radzir, S.A. Hanifah, A. Ahmad, N.H. Hassan, F. Bella, Effect of lithium bis (trifluoromethylsulfonyl)imide salt-doped UV-cured glycidyl methacrylate, J. Solid State Electrochem. 19 (10) (2015) 3079–3085, https://doi.org/10.1007/s10008-015-2910-z.

[11] K. Liu, Y. Liu, D. Lin, A. Pei, Y. Cui, Materials for lithium-ion battery safety, Sci. Adv. 4 (6) (2018), https://doi.org/10.1126/sciadv.aas9820.

[12] Y. hong Luo, et al., Nickel-rich and cobalt-free layered oxide cathode materials for lithium ion batteries, Energy Storage Mater. 50 (February) (2022) 274–307, https://doi.org/10.1016/j.ensm.2022.05.019.

[13] M.A.A.M. Abdah, et al., Synthesis and electrochemical characterizations of poly (3,4-ethylenedioxythiophene/manganese oxide coated on porous carbon nanofibers as a potential anode for lithium-ion batteries, Energy Rep. 7 (2021) 8677–8687, https://doi.org/10.1016/j.egyr.2021.10.110.

[14] X. Jiang, et al., The impact of electrode with carbon materials on safety performance of lithium-ion batteries: a review, Carbon N. Y. 191 (2022) 448–470, https://doi.org/10.1016/j.carbon.2022.02.011.

[15] L.H. Saw, Y. Ye, A.A.O. Tay, W.T. Chong, S.H. Kuan, M.C. Yew, Computational fluid dynamic and thermal analysis of Lithium-ion battery pack with air cooling, Appl. Energy 177 (2016) 783–792, https://doi.org/10.1016/j.apenergy.2016.05.122.

[16] T.M. Bandhauer, S. Garimella, T.F. Fuller, A critical review of thermal issues in lithium-ion batteries, J. Electrochem. Soc. 158 (3) (2011) R1, https://doi.org/10.1149/1.3515880.

[17] L. Lu, X. Han, J. Li, J. Hua, M. Ouyang, A review on the key issues for lithium-ion battery management in electric vehicles, J. Power Sources 226 (2013) 272–288, https://doi.org/10.1016/j.jpowsour.2012.10.060.

[18] Y. Fan, Y. Bao, C. Ling, Y. Chu, X. Tan, S. Yang, Experimental study on the thermal management performance of air cooling for high energy density cylindrical lithium-ion batteries, Appl. Therm. Eng. 155 (February) (2019) 96–109, https://doi.org/10.1016/j.applthermaleng.2019.03.157.

[19] Z. Wei, J. Hu, H. He, Y. Yu, J. Marco, Embedded distributed temperature sensing enabled multi-state joint observation of smart lithium-ion battery, IEEE Trans. Ind. Electron. (c) (2022), https://doi.org/10.1109/TIE.2022.3146503, 0046.

[20] D.I. Stroe, E. Schaltz, SOH estimation of LMO/NMC-based electric vehicle lithium-ion batteries using the incremental capacity analysis technique, 2018 IEEE Energy Convers. Congr. Expo. ECCE 2018 (Ic) (2018) 2720–2725, https://doi.org/10.1109/ECCE.2018.8557998.

[21] L. Sánchez, J. Otero, D. Anseán, I. Couso, Health assessment of LFP automotive batteries using a fractional-order neural network, Neurocomputing 391 (xxxx) (2020) 345–354, https://doi.org/10.1016/j.neucom.2019.06.107.

[22] Z. Wei, Z. Quan, J. Wu, Y. Li, J. Pou, H. Zhong, Deep deterministic policy gradient-DRL enabled multiphysics-constrained fast charging of lithium-ion battery, IEEE Trans. Ind. Electron. 69 (3) (2022) 2588–2598, https://doi.org/10.1109/TIE.2021.3070514.

[23] J. Wu, Z. Wei, W. Li, Y. Wang, Y. Li, D.U. Sauer, Battery thermal-and health-constrained energy management for hybrid electric bus based on soft actor-critic DRL algorithm, IEEE Trans. Ind. Inf. 17 (6) (2021) 3751–3761, https://doi.org/10.1109/TII.2020.3014599.

[24] A.K. Thakur, et al., A state of art review and future viewpoint on advance cooling techniques for Lithium–ion battery system of electric vehicles, J. Energy Storage 32 (April) (2020), 101771, https://doi.org/10.1016/j.est.2020.101771.

[25] D.K. Sharma, A. Prabhakar, A review on air cooled and air centric hybrid thermal management techniques for Li-ion battery packs in electric vehicles, J. Energy Storage 41 (May) (2021), 102885, https://doi.org/10.1016/j.est.2021.102885.

[26] T. Han, B. Khalighi, E.C. Yen, S. Kaushik, Li-ion battery pack thermal management: liquid versus air cooling, J. Therm. Sci. Eng. Appl. 11 (2) (2019), https://doi.org/10.1115/1.4041595.

[27] R. Sabbah, R. Kizilel, J.R. Selman, S. Al-Hallaj, Active (air-cooled) vs. passive (phase change material) thermal management of high power lithium-ion packs: limitation of temperature rise and uniformity of temperature distribution, J. Power Sources 182 (2) (2008) 630–638, https://doi.org/10.1016/j.jpowsour.2008.03.082.

[28] R. Mahamud, C. Park, Reciprocating air flow for Li-ion battery thermal management to improve temperature uniformity, J. Power Sources 196 (13) (2011) 5685–5696, https://doi.org/10.1016/j.jpowsour.2011.02.076.

[29] D. Chen, J. Jiang, G.H. Kim, C. Yang, A. Pesaran, Comparison of different cooling methods for lithium ion battery cells, Appl. Therm. Eng. 94 (2016) 846–854, https://doi.org/10.1016/j.applthermaleng.2015.10.015.

[30] X. Yu, Z. Lu, L. Zhang, L. Wei, X. Cui, L. Jin, Experimental study on transient thermal characteristics of stagger-arranged lithium-ion battery pack with air cooling strategy, Int. J. Heat Mass Tran. 143 (2019), 118576, https://doi.org/10.1016/j.ijheatmasstransfer.2019.118576.

[31] G. Zhao, X. Wang, M. Negnevitsky, H. Zhang, A review of air-cooling battery thermal management systems for electric and hybrid electric vehicles, J. Power Sources 501 (May) (2021), 230001, https://doi.org/10.1016/j.jpowsour.2021.230001.

[32] J. Xie, Z. Ge, M. Zang, S. Wang, Structural optimization of lithium-ion battery pack with forced air cooling system, Appl. Therm. Eng. 126 (2017) 583–593, https://doi.org/10.1016/j.applthermaleng.2017.07.143.

[33] S. Shahid, M. Agelin-Chaab, Development and analysis of a technique to improve air-cooling and temperature uniformity in a battery pack for cylindrical batteries, Therm. Sci. Eng. Prog. 5 (November 2017) (2018) 351–363, https://doi.org/10.1016/j.tsep.2018.01.003.

[34] X. Na, H. Kang, T. Wang, Y. Wang, Reverse layered air flow for Li-ion battery thermal management, Appl. Therm. Eng. 143 (July) (2018) 257–262, https://doi.org/10.1016/j.applthermaleng.2018.07.080.

[35] E. Jiaqiang, et al., Effects of the different air cooling strategies on cooling performance of a lithium-ion battery module with baffle, Appl. Therm. Eng. 144 (August) (2018) 231–241, https://doi.org/10.1016/j.applthermaleng.2018.08.064.

[36] R.D. Jilte, R. Kumar, L. Ma, Thermal performance of a novel confined flow Li-ion battery module, Appl. Therm. Eng. 146 (February 2018) (2019) 1–11, https://doi.org/10.1016/j.applthermaleng.2018.09.099.

[37] H. Zhou, F. Zhou, L. Xu, J. Kong, QingxinYang, Thermal performance of cylindrical Lithium-ion battery thermal management system based on air distribution pipe, Int. J. Heat Mass Tran. 131 (2019) 984–998, https://doi.org/10.1016/j.ijheatmasstransfer.2018.11.116.

[38] S. Gocmen, E. Cetkin, Emergence of elevated battery positioning in air cooled battery packs for temperature uniformity in ultra-fast dis/charging applications, J. Energy Storage 45 (2021) (June 2021), 103516, https://doi.org/10.1016/j.est.2021.103516.

[39] A. Bejan, S. Lorente, Design with Constructal Theory," *Design With Constructal Theory*, 2008, pp. 1–529, https://doi.org/10.1002/9780470432709.

[40] N. Yang, X. Zhang, G. Li, D. Hua, Assessment of the forced air-cooling performance for cylindrical lithium-ion battery packs: a comparative analysis between aligned and staggered cell arrangements, Appl. Therm. Eng. 80 (2015) 55–65, https://doi.org/10.1016/j.applthermaleng.2015.01.049.
[41] Z. Lu, X.Z. Meng, L.C. Wei, W.Y. Hu, L.Y. Zhang, L.W. Jin, Thermal management of densely-packed EV battery with forced air cooling strategies, Energy Proc. 88 (2016) 682–688, https://doi.org/10.1016/j.egypro.2016.06.098.
[42] T. Yang, N. Yang, X. Zhang, G. Li, Investigation of the thermal performance of axial-flow air cooling for the lithium-ion battery pack, Int. J. Therm. Sci. 108 (2016) 132–144, https://doi.org/10.1016/j.ijthermalsci.2016.05.009.
[43] MOLICEL®, PRODUCT DATA SHEET MODEL INR-21700-P42a," Maple Ridge, Canada, 2015 [Online]. Available: https://www.imrbatteries.com/content/molicel_p42a.pdf.
[44] T.F. Fuller, M. Doyle, J. Newman, Simulation and optimization of the dual lithium ion insertion cell, J. Electrochem. Soc. 141 (1) (1994) 1–10, https://doi.org/10.1149/1.2054684.
[45] "The k-ε Turbulence Model," COMSOL Multiphysics® v. 5.5. https://doc.comsol.com/5.5/doc/com.comsol.help.cfd/cfd_ug_fluidflow_single.06.088.html.
[46] COMSOL Multiphysics®, "COMSOL Multiphysics® v. 5.5." COMSOL AB, Stockholm, Sweden. [Online]. Available: www.comsol.com.
[47] H. Chen, et al., A simplified mathematical model for heating-induced thermal runaway of lithium-ion batteries, J. Electrochem. Soc. 168 (1) (2021), 010502, https://doi.org/10.1149/1945-7111/abd64c.
[48] S. Tiggelbeck, N.K. Mitra, M. Fiebig, Comparison of wing-type vortex generators for heat transfer enhancement in channel flows, J. Heat Tran. 116 (4) (1994) 880–885, https://doi.org/10.1115/1.2911462.
[49] A. Lemouedda, M. Breuer, E. Franz, T. Botsch, A. Delgado, Optimization of the angle of attack of delta-winglet vortex generators in a plate-fin-and-tube heat exchanger, Int. J. Heat Mass Tran. 53 (23–24) (2010) 5386–5399, https://doi.org/10.1016/j.ijheatmasstransfer.2010.07.017.
[50] B. Ghobadi, F. Kowsary, F. Veysi, Optimization of heat transfer and pressure drop of the channel flow with baffle, High Temp. Mater. Process. 40 (1) (2021) 286–299, https://doi.org/10.1515/htmp-2021-0030.
[51] S. Basu, et al., Non-isothermal electrochemical model for lithium-ion cells with composite cathodes, J. Power Sources 283 (2015) 132–150, https://doi.org/10.1016/j.jpowsour.2015.02.127.
[52] N.A. Chaturvedi, R. Klein, J. Christensen, J. Ahmed, A. Kojic, Modeling, estimation, and control challenges for lithium-ion batteries, Proc. 2010 Am. Control Conf. ACC 2010 (June 2010) (2010) 1997–2002, https://doi.org/10.1109/acc.2010.5531623.
[53] M. Safari, C. Delacourt, Modeling of a commercial graphite/LiFePO4 cell, J. Electrochem. Soc. 158 (5) (2011) A562, https://doi.org/10.1149/1.3567007.
[54] K.J. Lee, K. Smith, A. Pesaran, G.H. Kim, Three dimensional thermal-, electrical-, and electrochemical-coupled model for cylindrical wound large format lithium-ion batteries, J. Power Sources 241 (2013) 20–32, https://doi.org/10.1016/j.jpowsour.2013.03.007.
[55] V. Srinivasan, C.Y. Wang, Analysis of electrochemical and thermal behavior of Li-ion cells, J. Electrochem. Soc. 150 (1) (2003) A98–A106, https://doi.org/10.1149/1.1526512.